RESEARCH PAPER

Architecture-Driven Digital Volume Correlation: Application to the Analysis of In-Situ Crushing of a Polyurethane Foam

A. Rouwane[1] · P. Doumalin[2] · R. Bouclier[1,3] · J.C. Passieux[1] · J.N. Périé[1]

Abstract

Background Digital Volume correlation (DVC) consists in identifying the displacement fields that allow for the best possible registration of volume images of a sample captured at various loading stages. With cellular materials, the use of DVC faces an intrinsic limit: in the absence of an exploitable texture on (or in) the struts or cell walls, the available speckle pattern will unavoidably be formed by the material architecture itself. This leads to the inability of classical DVC techniques to measure kinematics below the cellular scale, *i.e.* at the sub-cellular or micro scales.
Objectives Here, we extend a newly developed architecture-driven DIC technique [1] for the measurement of 3D displacement fields in real cellular materials at the scale of the architecture.
Methods The proposed solution consists in assisting DVC by a weak elastic regularization using, as support, an automatic finite-element image-based mechanical model.
Results Complex (locally buckling) kinematics of a polyurethane foam under compression are accurately measured during an *in-situ* test. The method is essential to evidence the class of dominance (stretching versus bending) of the foam.
Conclusion The proposed method allows to confirm that the foam used is bending-dominated, which is not possible with a classical mesoscopic DVC approach. This method is a good candidate for the analysis of complex local deformation mechanisms at the architecture scale.

Keywords Digital volume correlation (DVC) · Multigrid image registration · X-ray microtomography · Image-based mechanical modeling · Mechanical regularization · Cellular materials · Polyurethane foam

✉ A. Rouwane
  rouwane@insa-toulouse.fr

  P. Doumalin
  pascal.doumalin@univ-poitiers.fr

  R. Bouclier
  bouclier@insa-toulouse.fr

  J.C. Passieux
  passieux@insa-toulouse.fr

  J.N. Périé
  jean-noel.perie@iut-tlse3.fr

1 Institut Clément Ader (ICA), Université de Toulouse, INSA-ISAE-Mines Albi-UPS-CNRS, Toulouse, France

2 Institut PPRIME, UPR CNRS 3346, Université de Poitiers, Chasseneui, France

3 Institut de Mathématiques de Toulouse (IMT), Université de Toulouse, UPS-UT1-UT2-INSA-CNRS, Toulouse, France

Introduction

Architected materials are excellent candidates for the design of multifunctional structures with outstanding specific properties [2, 3]. However, since such materials are characterized by the coexistence of, at least, two very different scales, the prediction of their mechanical behavior in non-linear regimes remains a challenge [4]. This is especially true for synthetic materials such as foams due to their random architecture. Indeed, the local response is obviously eminently linked to the local architecture. But the same type of question arises for additively manufactured materials, as the effect of defects induced by the process should be taken into account in the models [5, 6]. In this context, X-ray micro-computed tomography (μ-CT) emerges as an imaging modality perfectly adapted to the study of the behavior of such materials [7]. Specimen-specific image-based models can be built from volume images of a specimen which accounts for its actual geometric architecture and defects.

[8–13]. In addition, other images captured at different loading steps during *in-situ* testing [14] now provide access to valuable volumetric kinematic information using digital volume correlation (DVC) [15]. For instance, the exploitation of DVC displacement fields as boundary conditions in numerical simulation is essential to achieve a proper test/simulation comparison [16, 17]. Next, a strengthened DVC/simulation dialogue clearly opens the way to model validation [16, 18] and constitutive parameter identification [19, 20].

The most common approach to DVC remains the *local* or *subset-based* approach [15, 21]. It has the advantage of being highly parallelizable. However, the use of such an approach to establish the experiment/simulation link is tricky at the scale of architectural details especially in the non-linear regime. There are at least three reasons for this. First, the architecture does not provide sufficient grey-level distribution in general so that the architecture itself usually constitutes the only usable pattern for DVC. The minimum size of the subsets will then be limited by the characteristic length of the architecture. For example, for a cellular material, the minimum subset size will usually be of the order of the cell size. This constitutes a real bottleneck in terms of spatial resolution. The subset size will consequently be much larger than the element size used in the simulation.

Second, the generic shape functions used in the registration process are unlikely to correctly capture the actual complex kinematics which is strongly related to the underlying moving architecture. In foams, for instance, local crushing is common during compression tests [22]. Standard interpolation functions would then introduce a significant model error [1] as they are completely unable to consider such strong evolutions of the pattern. It would of course be possible to use incremental DVC [23], but this would induce a measurement bias and, probably, a larger number of tomographic acquisitions. Last, the process only gives access to a scattered displacement field at the subset centers. The connection with finite-element (FE) models is not direct. In the remainder, for the sake of simplicity, *mesoscale* will (abusively) refer to the scale of the cell, whereas *microscale* will correspond to the scale of the struts. While most of the existing DVC analyses are limited to mesoscale, to our knowledge, only one article reported an attempt to measure kinematics at the trabecula scale in a trabecular bone [24].

In order to bridge experiments and simulation more easily, another approach of the DVC, referred to as *global* or *FE-based*, was introduced [25]. It is particularly convenient in the sense that the same type of kinematic description as the one used in the simulation tools (*e.g.* usually finite elements) can be used directly in the measurement. However, as with the subset based DVC, for most cellular materials imaged by conventional μ-CT (i) the minimum element size for performing a FE-DVC measurement is limited by the characteristic size of the architecture and (ii) the usual FE

shape functions do not properly describe the underlying kinematics. While a refined image-based boundary fitted mesh would be convenient to describe the complex local kinematics, its direct use in standard FE-DVC would not be possible. This is because the elements would be too small with respect to the pattern and the vanishing of greyscale gradients within the elements would make the DVC problem ill-posed. However, global DVC has the advantage that it can be regularized *a priori*. Some authors have proposed, for instance, to use regularization schemes, based on second-order Tikhonov operators, to compensate the lack of texture in cellular materials such as trabecular bone [26].

In the following, we extend the approach introduced and validated in 2D digital image correlation (DIC) in [1] to the DVC analysis of a complex *in-situ* compression test on a polymeric foam. This method consists in imposing that the sought-after micro displacement field should be mechanically consistent [27, 28]. A weak regularization based on a Tikhonov approach [29, 30] is thus used based on the equilibrium gap [31]. The weight given to the mechanical part introduces a characteristic length of regularization below which the mechanical part takes precedence, while above it the image pulls the correlation.

In other existing mechanically regularized DVC approaches, it is common to rely on macroscopic (or homogenized) models whose mesh does not conform with the micro-structure [32]. The subsets or finite elements are larger than the architecture scale which usually does not allow for a proper representation of the underlying micro kinematics. Conversely, the proposed approach aims at estimating complex local kinematics at the scale of the architecture of the material with no *a priori* on the model or on the geometry of the sample. In other words, our assumption is that the grey levels carry a mechanical information that is used to help regularize DVC. It is a challenge when working with random architecture materials like foams since the geometry is specific to the sample and most importantly unknown. It thus requires fine meshing strategies to build a sample-specific image-based geometric and mechanical model at the architecture scale (*i.e.*, describing a representative architecture) from the images. In addition to the regularization length and the choice of the mechanical modelling (and boundary conditions), the choice of the parameters of the geometric modelling (threshold, mesh size) has to be done carefully as a trade-off between computational cost and mechanical approximations. This work done in 2D-DIC [1] has shown that by choosing correctly these parameters with the general rules (length of regularization related to the size of the cell, fineness of the mesh fixed compared to the size of the pixel), the method was able to capture complex non-linear local phenomenon (despite the simple behaviour assumption). In this work, we generalize the previous 2D study of [1] to 3D. The potential of this extension is

highlighted by measuring the locally complex 3D kinematics resulting from crushing in a polyurethane foam subjected to an *in-situ* compression test. The presented experiment and the corresponding image set are very challenging for DVC analysis because the texture deforms at a scale smaller than the subset (or element) size. The obtained displacement fields are compared to those provided by standard mesoscale regularized FE-DVC approach. The level of deformations between the reference image (taken at rest) and the following images is such that a particular strategy is necessary to initialize DVC. Moreover, as microscale DVC measurements require high hardware resources, a high performance parallel implementation is required.

Cellular or porous architected materials have two main deformation modes depending on the nature of their local architecture. Indeed, depending on whether they are *stretching-dominated* or *bending-dominated*, their macroscopic behavior, their stiffness and their use differ significantly [33, 34]. Indeed, bending-dominated materials form the majority of materials and particularly foams. Stretching-dominated materials have a much higher specific stiffness. We show that the proposed DVC method contributes to better analyzing in the bulk the nature (bending versus stretching dominance) of crushing mechanisms inside open cell polymeric foams.

Sample, Experiment and Instrumentation

Material, Specimen and Motivations

The selected porous material is a polyurethane foam. The *in-situ* tests carried out in the X-ray μ-CT scanner and presented hereafter aim at identifying the spatial distribution of the mechanical properties in relation with the local architectural properties (*e.g.* the local porosity). One first step towards realizing this long term objective is to incorporate a DVC analysis in the identification framework. The main purpose of this work is to raise the challenge of measuring displacement fields at the scale of the architecture in real-word cellular materials. The foam had a porosity $V(void)/V(total)$ equal to 0.96. The mean diameter of the cells was 500 μm with a standard deviation of ± 200 μm. As illustrated in Fig. 1, the tested sample had a cylindrical shape with a diameter of 9 mm and a height of 10 mm.

Experiment and μ-CT Acquisition

A compression machine was specifically designed and used in order to perform the *in-situ* test (see Fig. 2). For this setup, an electric cylinder was used in order to apply the mechanical load. The capacity of the load cell used was 50 N. A reference scan was carried out, specimen mounted,
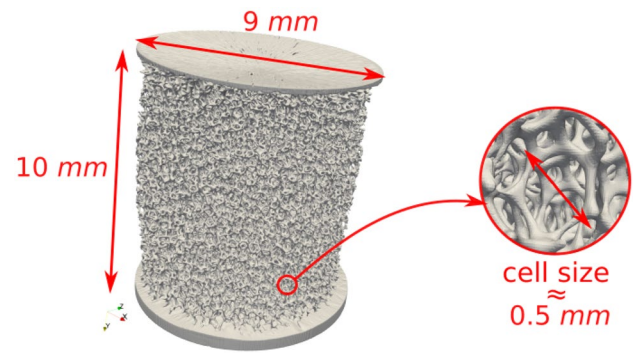

Fig. 1 Physical dimensions of the chosen cellular sample

before starting the test. Then the loading was interrupted several times in order to allow the sample to be scanned. Each scan lasted approximately 40 to 50 min. The four stages of loading considered corresponded to an overall strain of the order of 3.4%, 5.2%, 12.3% and 28.5%.

In total, the starting point of our DVC analysis is the five reconstructed volumes of the foam (*i.e.* the image of the reference configuration denoted I_r and the four images of the deformed configurations denoted I_d). Figure 3 shows the rendered volumes of these configurations. The visualization of the different loading states is performed using the Paraview software [35, 36]. It takes, in this case, as input, the different VTU (Unstructured VTK) files of the surface representation of the segmented volume. Finally, the different parameters of the μ-CT acquisition are synthesized in Table 1.

DVC Methodology

In this work, we will carry out two types of analysis. The first one, referred to as mesoscale DVC, can be seen as the classic approach in the field. It makes use of a global DVC approach [25] based on rather coarse and regular meshes of the whole specimen,
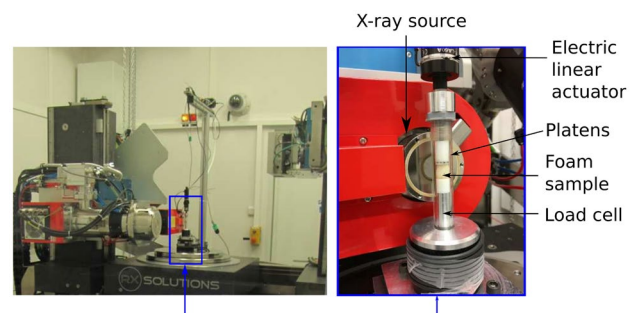

Fig. 2 Experimental setup of the *in-situ* compression test using X-ray μ-CT

Table 1 DVC acquisition parameters

Parameters	Information
CT device	Ultratom RX solutions
Source	230kV
Voltage	50kV
Current	200μA
Detector	Varian 3 Mpixels
Encoding	16 bits
Memory size of one reconstructed scan	7.6 GB
Definition	$1523 \times 1514 \times 1654$
Number of scans	5 (1 Reference + 4 loadings)
Duration of each scan	45 min
Voxel size	6.67 μm
Target	Reflexion target
Filter	None
Tube to detector	865.6 mm
Source to object	35.5 mm
Number of projections	1600
Angular amplitude	360°

i.e. that each element includes several cell-struts and void of the foam. The second approach, which is the microscale DVC developed in this paper, consists in an extension of the method proposed in [1]. It relies on weak mechanical regularization [27, 28, 37, 38] and image-based modeling [9, 11]. It benefits from the construction of a fine FE mesh that properly describes the architecture of the foam. In this section, we start by outlining the fundamental aspects behind DVC and then more precisely introduce the mesoscale and microscale DVC methods.
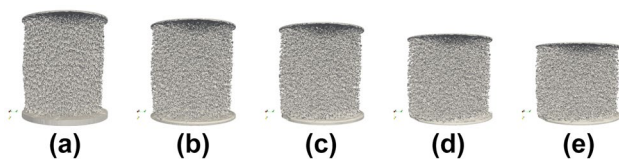
Fundamental Aspects

Grey-level metric

Given two grey-level images I_r and I_d representing, respectively, the reference and deformed configurations of a material sample, DVC can formally be expressed as the following optical flow equation [39]:

$$\text{Find} \quad u : \Omega \subset \mathbb{R}^3 \rightarrow \mathbb{R}^3, \quad \text{such that}$$
$$I_r(\mathbf{x}) = I_d(\mathbf{x} + u(\mathbf{x})), \quad \forall \mathbf{x} \in \Omega. \tag{1}$$

Fig. 3 Rendering of the reconstructed volumes at the different loading states. (**a**) Reference configuration and (**b-e**) Deformed configurations

x defines the point coordinates in the reference region of interest Ω included in the initial reconstructed volume. It was underlined in [40] that the formulation (equation (1)) is a Lagrangian description of the optical flow while the formulation which would consist in defining **x** in the deformed configuration would be an Eulerian one. The grey-level conservation problem is generally ill-posed as it consists in reconstructing a three-dimensional field only using a noisy scalar grey-level field. Therefore, problem (equation (1)) is rather solved by minimizing a global grey-level metric that can be chosen as the squared quadratic norm of the residual of grey-levels. In addition, the unknown displacement field is discretized by means of a set of basis functions. Overall, the DVC problem can be written as:

$$\min_{\mathbf{u} \in \mathbb{R}^{ndof}} S(\mathbf{u}) = \int_\Omega \left(I_r(\mathbf{x}) - I_d(\mathbf{x} + \mathbf{N}(\mathbf{x})\mathbf{u}) \right)^2 d\mathbf{x}, \tag{2}$$

where $\mathbf{N}(\mathbf{x}) \in \mathbb{R}^{3 \times ndof}$ is the considered shape functions matrix and $\mathbf{u} \in \mathbb{R}^{ndof}$ is the vector that gathers the total (*ndof*) degrees of freedom (DOF). In this work, we will consider FE-DVC [25, 27, 38, 41] since this is the starting point to regularize DVC using a mechanical knowledge of the solution. The shape functions gathered in $\mathbf{N}(\mathbf{x})$ are thus associated to a FE mesh which will be composed of 4-node (linear) tetrahedral finite elements.

Optimization scheme

In the DIC community, problem (equation (2)) is usually solved using a modified Gauss-Newton algorithm [42, 43] which leads to the following iterative scheme. Given an initial displacement guess $\mathbf{u}^{(0)}$, the solution $\mathbf{u}^{(k)}$ at iteration k is updated such as:

$$\mathbf{u}^{(k+1)} = \mathbf{u}^{(k)} + \mathbf{d}^{(k)} \quad \text{with} \quad \mathbf{H}_S \, \mathbf{d}^{(k)} = \mathbf{b}(\mathbf{u}^k)$$
$$\text{and} \quad \mathbf{b}(\mathbf{u}^k) = -\nabla S(\mathbf{u}^{(k)}). \tag{3}$$

$\nabla S(\mathbf{u}^{(k)})$ and $\mathbf{H}_S$ are the modified gradient and Hessian matrix of S, respectively, that involve the gradient of the reference image I_r only. For more details regarding the algorithm and implementation, the reader is referred to, *e.g.*, [41–43].

It must be stated, at this stage, that system (equation (3)) may be singular if the image gradient vanishes within the finite elements [44]. That is why a high frequency black and white speckle pattern is usually sprayed on the specimen surface in 2D-DIC [45–47]. This issue is central in DVC since it is hardly possible to add artificial speckle patterns in volume imaging [48, 49]. There are basically two ways of performing DVC in such situations: *strong* or *weak* regularization. The first one aims at reducing the number of unknowns by either increasing the size of the

elements [15, 25, 50] or projecting the problem onto an appropriate reduced basis [51–53]. The second approach consists in adding a penalization term to functional (equation (2)) in order to improve its convexity [1, 26–28, 37, 38, 54–57]. Both approaches aim at reducing the apparent dimension of the minimization subspace of problem (equation (2)). In the following, the mesoscale analysis will make use mainly of a strong regularization with coarse FE meshes whereas the microscale analysis will rely on a fine-tuned weak elastic regularization based on the construction of a fine FE mesh that properly describe the architecture of the material.

Sub-voxel evaluation

In order to evaluate functional (equation (2)) and build the operators in (equation (3)), the sub-voxel grey-level evaluation of the images is necessary. In this work, this is performed using a B-spline representation of the volume images [58, 59]. It consists in computing a new regular function $\widetilde{I}$ defined as:

$$\widetilde{I}(x,y,z) = \sum_{i=1}^{l} \sum_{j=1}^{m} \sum_{k=1}^{n} B_{i,p}(x)B_{j,p}(y)B_{k,p}(z)\mathbf{c}_{i,j,k}, \tag{4}$$

where $B_{i,p}$, $B_{j,p}$ and $B_{k,p}$ are the total l, m, n univariate B-spline functions of degree p centered at each voxel. (x, y, z) is a non integer point in the image domain $[0, l] \times [0, m] \times [0, n]$. The tensor $\mathbf{c} \in \mathbb{R}^{l \times m \times n}$ represents the voxel grey-level values. We should note that this image representation is not interpolatory but has the advantage of preserving the image dynamic and removing the oscillatory effects of global polynomial interpolation [58]. It has also the advantage of not pre-computing interpolation coefficients which usually requires the inversion of linear systems. The image gradients are also computed by simply differentiating (equation (4)). This provides regular gradient fields even when the texture of the considered specimen is poor.

Analysis of the correlation

In order to assess the quality of the correlation at convergence, the grey-level residual field is a very interesting quantity to analyse. It is defined as follows:

$$r(\mathbf{x}) = I_r(\mathbf{x}) - I_d(\mathbf{x} + u(\mathbf{x})), \quad \forall \mathbf{x} \in \Omega. \tag{5}$$

From (equation (5)), it is possible to build a global indicator equal to the standard deviation of the distribution r. It is also very instructive to plot its distribution on the material architecture to provide more information on the localization of the potential mismatch.

Mesoscale DVC

When considering the global FE-DVC methodology, the finite-element size is crucial and conditions the accuracy of the correlation. Since the texture in DVC is necessary associated to the scale of the material constituents, large finite elements are defined so that each point in the images is tracked along with its close neighborhood. As stated before, the mesoscale DVC analysis is performed mainly with the help of a strong regularization where the finite-element size controls the amount of regularization. More precisely, each element must contain sufficient grey-level variations, such that operator $\mathbf{H}_S$ is not singular [44].

In practice, the size of the elements can be related to the cell size of the material. Indeed, the finite elements need to be sufficiently large to include several struts, *i.e.* several speckle dots as prescribed in the literature [60]. The approximate cell size was first determined using the normalized radially averaged auto-correlation function (see Fig. 4(a)).

The presence of a secondary peak in this function is evidence of a pseudo-periodicity in the image texture. The position of this secondary peak is thus considered as an approximation of the cell size, see the red dot in Fig. 4(a). In our case, the value of 28 voxels was obtained which agrees with the experimental value of 500 μm for the mean cell size (see Fig. 4(b)).

Here, we rely on a cylindrical FE mesh of the whole material sample based on tetrahedral meso elements that include both struts and voids. Figure 5 shows the three mesh discretizations that were considered with an average element size of 33, 23 and 12 voxels, respectively. Note that only the coarsest mesh was such that the size of the elements exceeded that of the cells which is required to perform a correlation with strong regularization alone. The two finer meshes actually required the combined use of an additional weak regularization (Laplacian-based diffusion regularization technique). More details about weak regularization will be given in "Elastic Regularization".
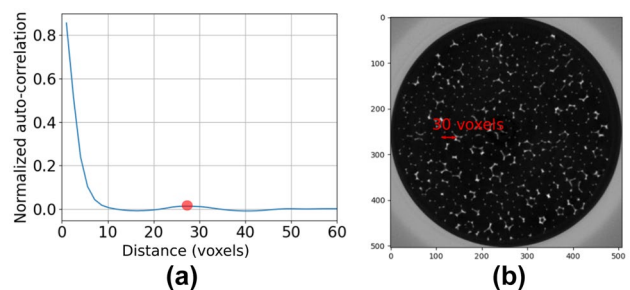
Fig. 4 Determination of the approximate cell size using the radially averaged normalized auto-correlation function. (**a**) Auto-correlation function in the reference image that exhibits a secondary peak around 28 voxels (red dot) and (**b**) Slice of the reconstructed volume stack
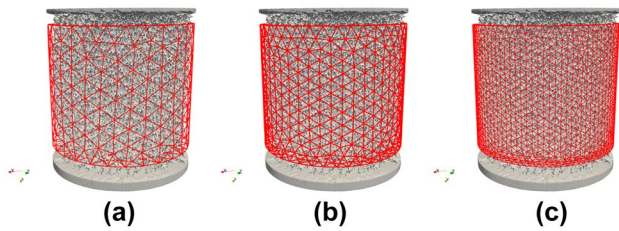
Fig. 5 Three finite element mesoscale DVC discretizations. (**a**) 33 voxels, (**b**) 23 voxels and (**c**) 12 voxels

A very important aspect in image correlation is the determination of the initial displacement guess. For the two first loading states (see Fig. 3 again), the initial displacement $\mathbf{u}^{(0)}$ was set to zero and then a coarse-to-fine scheme based on four levels of image binning was performed for the initialization. This technique also known as multi-level (or multi-grid) initialization consists in constructing a pyramidal refinement strategy for both the image and measurement resolutions. The interested reader can find more details about these strategies in [41, 61–65] to name a few. Roughly speaking, this process allows to gradually filter the high-frequency components of the image so that the convexity support of functional (2) is increased at the coarser levels. This helps solving the minimization problem with an arbitrary initialization. However for the third and fourth loading states, this strategy was not sufficient to make converge correctly the Gauss-Newton algorithm. One successful strategy consisted in using a structured mesh with few elements in the height direction and running a DVC (also initialized with a coarse-to-fine strategy) to estimate a first coarse displacement. This structured mesh, displayed in Fig. 6, covered the whole image domain (including a part of the bottom and top platens). The image signal given by the bottom and top platens helped the correlation algorithm as they were subject to translation during loading. To summarize, the first step of the correlation is performed with the mesh presented in Fig. 6 (hexahedral FE this time).

The obtained displacement is then evaluated at the nodes of the tetrahedral finite element meshes of Fig. 5 in order to get the initial guess denoted $\mathbf{w}$. Finally, in order to correctly re-scale this initial guess, an additional tiny correlation (that converged in three iterations) was performed using a reduced basis approach. In this case, the displacement increment $\mathbf{d}^{(k)}$ was searched for as a projection onto a reduced basis. Let us denote $\mathbf{R}$ the matrix gathering the reduced basis vector in column, in this case it is computed as follows:

$$\mathbf{d}^{(k)} = \mathbf{R}\,\boldsymbol{\alpha}^{(k)} \quad \text{with} \quad \mathbf{R}^T \mathbf{H}_S \mathbf{R}\,\boldsymbol{\alpha}^{(k)} = \mathbf{R}^T \mathbf{b}^{(k)}. \tag{6}$$

where $\boldsymbol{\alpha}^{(k)}$ are the scaling modes. The scaling matrix was defined as follows:
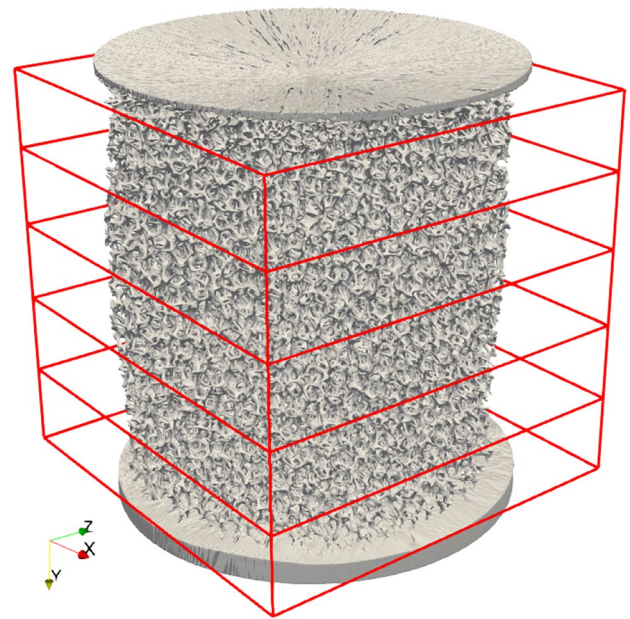
Fig. 6 Coarse grid used for the determination of an initial displacement guess

$$\mathbf{R} = \begin{pmatrix} \mathbf{w}_x & \mathbf{0} & \mathbf{0} \\ \mathbf{0} & \mathbf{w}_y & \mathbf{0} \\ \mathbf{0} & \mathbf{0} & \mathbf{w}_z \end{pmatrix} \in \mathbb{R}^{ndof \times 3}. \tag{7}$$

$\mathbf{w}_x$, $\mathbf{w}_y$ and $\mathbf{w}_z$ are the vector displacement blocks extracted from $\mathbf{w}$ (corresponding to the x, y, z directions, respectively). $\mathbf{0}$ is a zero vector of size $ndof$.

Microscale DVC

The mesoscale approach of the previous section relies on coarse meshes which can only estimate displacement fields that are homogenized at the scale of the cells. As will be shown in the examples, the use of large elements that include both struts and voids, makes it impossible to properly describe the highly complex local kinematics that occur during the compression test (large deformations or (post) buckling of the struts).

It this section, the microscale DVC approach is detailed. Microscale means that we aim at measuring the kinematic transformation at the scale of the struts (or the architecture). For that, we will extend the recently developed approach [1] for the measurement of 3D displacement fields. Briefly, two important ingredients are required. The first one is the use of an image-based FE mesh [9, 11] that properly describe the architecture of the material. This mesh is thus boundary-fitted at the architecture scale. The use of such a fine mesh is required to well describe the complex displacements of the struts but is not compatible with DVC since the grey-level distribution within the mesh is almost homogeneous or in
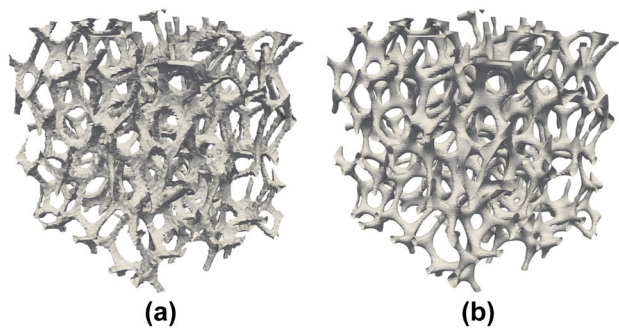
Fig. 7 Surface representation of the cellular geometry using a low resolution image ($50 \times 50 \times 50$). (**a**) Without the Gaussian blur and (**b**) with the Gaussian blur with a kernel of 2 voxels (this value was exaggerated for visualisation purposes, in the analyses it was set to 0.8 voxel)

Fig. 8 Position and definition of the region of interest (in blue color) considered in the microscale DVC. In grey color: all the foam domain

other words, its gradient is almost zero. To solve this issue, the second ingredient consists in adding a weak elastic regularization [27, 28, 37, 38, 54, 57, 66] using the previously image-based FE model whose geometry (and thus stiffness) is relevant at the architecture scale.

Image-based mesh generation

Image-based mesh generation consists in automatically constructing a FE mesh from the voxel data. In general, the steps of this approach are: (i) segmentation which consists in classifying each component of the material, (ii) boundary definition and finally (iii) volumetric meshing. In this work, segmentation is quite immediate as the foam is assumed to be composed of only void and solid. Therefore, the domain of interest is entirely described by one grey-level threshold value. This value used for both rendering and mesh generation was optimized using a bisection algorithm so that the porosity of the segmented geometry reaches the porosity value 0.96 given by the supplier. This led to take $\gamma = 56$. In order to smoothly describe the boundary of the cellular geometry, Gaussian filtering was also performed. The new grey-level values were defined by the convolution:

$$\mathbf{c} = G_\sigma * I, \tag{8}$$

where I is the reconstructed volume and G_σ is a Gaussian kernel (σ, the standard deviation, was chosen equal to 0.8). A value smaller than the threshold value was assigned to the grey-level field at the top and bottom boundaries of the region of interest so that a closed watertight region was obtained. Surface extraction was then performed using the marching cubes algorithm [67] available in the scikit-image Python library [68]. Figure 7 illustrates the effect of Gaussian blurring on the smoothness of the cellular geometry. This procedure allows to reduce the geometric modeling error and
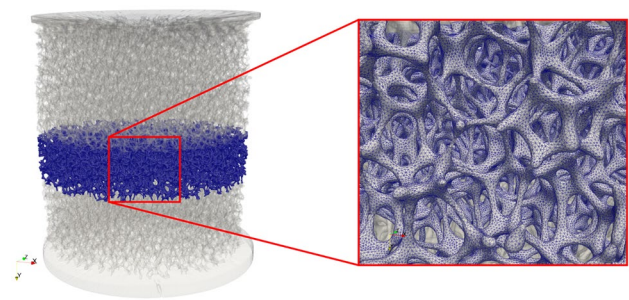
therefore improves the accuracy of the measured fields. We note that the mesh generation procedure is performed on the $2 \times 2 \times 2$ binned image of the reference configuration in order to reduce the memory footprint.

A region of interest was extracted from the whole foam volume (see Fig. 8(left)). The idea here is to use the microscale approach only in a region where highly localized phenomena occur (*i.e.* where the grey-level mismatch is high). We chose to extract a slice from the volume of the reference configuration I_r. This full cylindrical slice has a volume of 17.865 million of voxels cube (more exactly a radius of 240 voxels and a height of 100 voxels). Figure 8 shows again the extracted slice from the cylindrical volume in addition to its finite element mesh. The mesh was generated using the CGAL library [69] which provides the user to choose the mean finite element face's size. The process took 30 minutes to be completed. 91 isolated connected components (isolated voxels or groups of voxels) were removed in a first mesh cleaning step. The obtained mesh has 3 660 568 elements and 1 212 616 nodes. The average element volume is around 0.34 voxels cube, which corresponds to an average element size of 0.7 voxels.

Now that the geometric characterization of the cellular architecture has been presented, the use of such fine description of the cells as a direct support for the DVC measurements is presented hereafter.

Elastic regularization

As stated above, the strong regularization based on the FE discretization becomes obsolete if one considers solving the DVC problem (equation (2)) with the microscale FE mesh depicted in Fig. 8(right). In particular, this unavoidably makes the correlation matrix $\mathbf{H}_S$ in (equation (3)) singular. As a first remedy, one could use, for instance, the Levenberg-Marquardt algorithm with an update strategy for stabilizing the Hessian matrix [70]. However, this lacks of physical meaning and thus will not provide relevant derivative fields (such as strains and stresses) within the cell-strut.

Here we rather resort to mechanical regularization. More precisely, similarly as in [1], we add a penalty term to the functional (equation (2)). It enforces weakly the internal elastic equilibrium of the material at the architecture scale by making use of our previously constructed microscale FE mesh. The strategy is further outlined in the following and we refer the interested reader to [1] for additional details on the approach.

From a fundamental point of view, a very rich survey of such Tikhonov-based regularization strategies can be found for example in [29, 30]. The general discrete optimization form is given by:

$$\min_{\mathbf{u}\in\mathbb{R}^n} S(\mathbf{u}) + \lambda\,\mathbf{u}^T\mathbf{T}\,\mathbf{u}, \tag{9}$$

where $\mathbf{T}$ is a linear operator and λ is a weighting parameter. The presence of a FE discretization offers a great flexibility as it allows to directly construct differential operators in $\mathbf{T}$ coming from physical models. For the coarse FE meshes of Fig. 5(b-c) (*i.e.*, for the mesoscale DVC), the measurement was regularized using the diffusion model which consists in setting $\mathbf{T} = \mathbf{L}$ with $\mathbf{L}$ the Laplacian operator [39, 55]. For the microscale DVC (*i.e.*, associated to the fine FE mesh of Fig. 8(right)), we make use of an elastic kernel for the regularization.

Pioneering works [61, 71] considered the elastic energy, *i.e.* equal to $\frac{1}{2}\mathbf{u}^T\mathbf{K}\mathbf{u} - \mathbf{u}^T\mathbf{f}$ where $\mathbf{K}$ and $\mathbf{f}$ are respectively the FE stiffness matrix and external force vector. This regularization introduces too much *a priori* and thus filters too much the displacement fluctuations. Instead, we rather increase the order of the regularization operator by considering the squared quadratic norm of the elastic equilibrium gap $\mathbf{K}\mathbf{u} - \mathbf{f}$ [31]. This approach was introduced in [28] where it was used for the identification of cracks in a silicon carbide specimen. It was later applied for DVC in particular in [27, 38] where a physical interpretation of the regularization parameter λ was established. The advantage of the latter regularization is that it is a fourth-order filter. It is consequently a smoother regularization compared to the model based on the elastic energy.

Very recently, and in the same spirit as in this work, this regularization was used for DVC measurements in heterogeneous materials, for example in [57] where the damage in mortar was quantified, and in [66] where a printed pantographic metamaterial was studied. Now, based on the proof-of-concept given in [1] for 2D-DIC, the purpose is to make use of this regularization scheme for microscale DVC measurement in cellular materials with complex and arbitrary topologies.

Another advantage of the equilibrium gap regularization over the one based on the energy is the possibility to remove the contribution of the regularization onto the Dirichlet and non-zero Neumann boundaries, *i.e.* where $\mathbf{f}$ does not vanish.

Indeed, when choosing a region of interest inside the volume, the external force vector $\mathbf{f}$ is unknown in practice at the non-free surfaces (we may barely access to one resultant if the volume is completely cut in one direction). As a consequence, the equilibrium has to be prescribed only at the nodes of the bulk and at free boundaries. To do so, we simply introduce a binary selection operator $\mathbf{D}_K$ that selects theses nodes. As the remaining nodes are removed from the regularization, they are guided only by the correlation. This can lead to a very irregular solution when the element size is very small, which is the case in this study. That is why a curvature regularization of the Dirichlet/non-zero Neumann boundaries is considered for these nodes. In other words, in the part where no relevant physical information is available, we perform a curvature-based regularization, and in the remaining domain where the discrete mechanical equilibrium can be safely formulated, a mechanically regularized DVC based on an elastic kernel is performed. From a mathematical viewpoint, by introducing the complementary selection operator $\mathbf{D}_L$, we end up with the following normalized optimization functional [27]:

$$\min_{\mathbf{u}\in\mathbb{R}^{ndof}} \frac{S(\mathbf{u})}{S(\mathbf{v})} + \lambda_K \frac{\|\mathbf{D}_K\mathbf{K}(E=1,\nu)\mathbf{u}\|_2^2}{\|\mathbf{D}_K\mathbf{K}(E=1,\nu)\mathbf{v}\|_2^2} + \lambda_L \frac{\|\mathbf{D}_L\mathbf{L}\mathbf{u}\|_2^2}{\|\mathbf{D}_L\mathbf{L}\mathbf{v}\|_2^2}, \tag{10}$$

where λ_K and λ_L are the regularization parameters for the bulk and the non-free boundaries respectively. Note that Young's modulus E for the elastic, isotropic and homogeneous regularization model at the architecture scale is fixed to 1 as $\mathbf{K}$ is proportional to E. The normalization of the functional is performed using a trial shear wave displacement field $\mathbf{v}$ which allows to relate the regularization parameters to its period. It can be defined for example by $\mathbf{v} = (\mathbf{0}, \cos(\frac{2\pi}{T}\mathbf{y}), \mathbf{0})$. It has been highlighted in [27] that regularizing DVC using the quadratic norm of the operators $\mathbf{L}$ and $\mathbf{K}$ can be seen as a fourth-order low-pass filter acting on the measured displacements on both the bulk and boundary regions. The regularization weights λ_K and λ_L can be related to cut-off characteristic lengths denoted l_K and l_L, respectively, which verify:

$$\lambda_K = \left(\frac{l_K}{T}\right)^4, \quad \lambda_L = \left(\frac{l_L}{T}\right)^4. \tag{11}$$

It has been highlighted in [1] that the optimal cut-off wavelength l_K in our case of cellular materials can be approximately set to the cell size. This emanated from a parametric L-curve study performed on an artificial 2D foam-like specimen.

The latter study has shown that the term associated with the grey-level residuals in (equation (10)) captures the low frequency part of the solution, *i.e.* associated with the mesoscale, while the local part of the displacement, *i.e.* below

the cell scale or at the microscale, is driven by the regularization that prescribes a locally elastic behavior. This makes sense in continuum mechanics and will allow to measure inealistic fields, such as large deformations of the struts, as will be seen in "Analysis of Result". The values for the other parameters (Poisson ratio ν and boundary regularization length l_L) of the regularized scheme (equation (10)) will be indicated and discussed in "Microscale DVC Results and Comparison With Mesocate DVC".

It is worth noting that the mechanically regularized approach increases significantly the numerical cost of DVC as we add to the correlation Hessian $\mathbf{H}_S$ a matrix that has the same pattern as $\mathbf{K}^T\mathbf{K}$. The higher the regularization order, the denser the correlation linear system as the number of extra diagonals increases. From a general viewpoint, our implementation of microscale DVC which consists in performing classical FE assemblies over the whole domain, cannot be seen as the solution for treating large scale problems. The mesoscale and microscale DVC are two complementary approaches that should be used concurrently, for instance in a multiscale framework. As a first step, the mesoscale DVC will allow to initialize the microscale DVC in this work.

The microscale approach will be applied to the region of interest defined in Fig. 8. The idea, again, is not to apply the weak elastic regularization scheme on the whole image domain but only on the targeted slice. The microscale approach allows to remove all the voxels in the voids from the computation and as the considered foam is very porous (*i.e.* there is far more void than material), the microscale DVC allows to treat only 3.6 million fine tetrahedral elements that represent the micro-architecture. If the whole volume would be registered (as it is the case for dense optical flow measurements), 17.8 million voxels would have been treated.

Special care for the foam specimen

After meshing the region of interest, the regularization strategy for the boundary surfaces must be defined. As we consider a compression test, and since the specimen is cylindrical, the side surface of the slice should be free. In the experimental setup, the foam sample is put inside a rigid transparent polymeric tube that plays the role of the load frame (see Fig. 2 right). Here, the internal diameter of the tube is the result of a compromise aimed on the one hand at minimizing the scan resolution (because of the cone beam technology, the X-ray source - sample distance must be minimized) and on the other hand at leaving a functional clearance (to get the sample move laterally). This solution has the merit of simplifying the setup of the reconstruction. If the lateral movements of the sample was not hindered, the side would be free. Figure 9(a) illustrates the corresponding boundary conditions if the external boundary was free
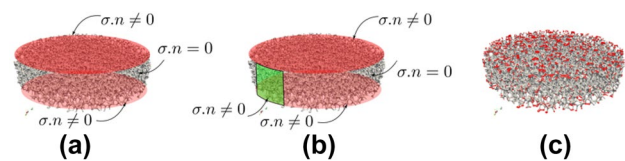
Fig. 9 Description of the boundary regularization applied on the extracted foam slice. (**a**) Ideal boundary conditions, (**b**) Experimental boundary conditions: contact occurs with the compressive cylinder in the green region and (**c**) Nodes penalized with the curvature regularization

during loading. In reality, this hypothesis is not verified. Unfortunately, during loading, contact occurs between the loading cylinder and the external boundary of the foam sample (see the green region in Fig. 9(b)). In order to avoid making the hypothesis of traction free in regions where it is not the case, we decide to penalize the nodes that belong to the external boundary in addition to the top and bottom nodes (as shown in Fig. 9(c)).

Finally, concerning initialization, the first displacement guess is projected from the mesoscale DVC solution. In order to do so, a strategy of displacement exchange between two arbitrary FE meshes has been incorporated. In order to project the displacement field from the coarse mesh to the fine mesh, one needs to determine in which elements of the coarse mesh belong the nodes of the fine mesh so that the FE interrogation (interpolation) is performed. The practical resolution of this geometric problem is summarized in Appendix.
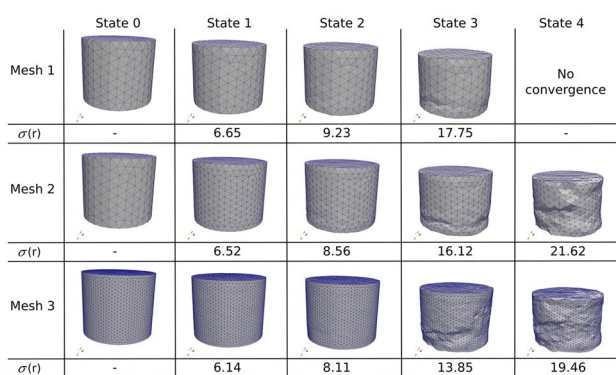
Analysis of the Results

The following numerical computations were performed on a 64-bit station equipped with Intel Xeon(R) CPU E5-2637 v2 processor (3.5 GHz frequency, 16 CPUs), 125.8 GB of RAM. The parallel assembly routines were computed over the 16 CPUs using OpenMp directives. Concerning the linear system solution, as the numerical solvers were used as a black box and no further investigation concerning this aspect was performed, the CHOLMOD direct solver [72] provided by the Python scikit-sparse library exploited only 8 CPUs on this same machine. The different parameters for the different DVC analyses are synthesized in Table 2. The so-called ultimate error was estimated using synthetic images with sub-pixel shifts using 3D FFT. The reported values are in good agreement with the *a priori* estimates calculated after [38]. However, these values should be considered as a lower bound of measurement uncertainty, as they do not take into account the model error. Further analysis on measurement errors with such an approach, was carried out in [1].

Table 2 Summary of the DVC parameters for the computations

Parameters	Mesoscale DVC				Microscale DVC
	Mesh 1	Mesh 2		Mesh 3	Mesh 4
Mean element length (voxels)	33	23		12	0.7
Matching functional		Equation (9) with $\mathbf{T} = \mathbf{L}$			Equation (10)
Regularization length (voxels)	$l_L = 0$	$\lambda = 10^2 (l_L \approx 35)$			$l_K = 35, l_L = 35$
Ultimate error (voxels)	3.16×10^{-4}	6.90×10^{-4}		8.16×10^{-4}	2.57×10^{-4}
Initialization		Coarse to fine			Solution of mesh 3
FE type		4 node tetrahedrons (Lagrange)			
Mesh geometry		Figure 5			Figure 8
Image definition (voxels^3)		$507 \times 504 \times 551$ (Binning of a factor 3)			
Sub-voxel evaluation		B-spline (equation (4)) with $p = 3$			
Gaussian pre-filtering kernel (voxels)		$\sigma = 0.8$ (equation (8))			

Mesoscale DVC Results

The mesoscale DVC approach allowed to obtain the final measurements displayed in Fig. 10. This same figure also shows the global residual indicators obtained for the different correlations. The first mesh resolution of 33 voxels failed for the last loading state. It clearly shows that the finer the discretization is chosen, the better the correlation is which is an obvious expectation in image correlation, provided that a well-suited weak regularization is employed. For the fourth loading state, the correlation algorithm converged probably to a local minimum (because the correlation score is very high). A very large strain can be reported (28.5%). This highlights the limit of the correlation approach when choosing relatively large discretizations. For the first and second loading states, as we are still in the linear regime, the correlation based on large elements allowed to get a "good" correlation score which was not the case for the third and fourth states. The corresponding measured displacement fields are shown in Fig. 11 for completeness. Overall, this first study based on meso elements confirms the limits of a classical FE-DVC approach (classical in the sense that it is equivalent to a mesoscale subset DVC approach).

Microscale DVC Results and Comparison With Mesocale DVC

Parameter set-up

As indicated in "Elastic Regularization", the optimal regularization length l_K can be chosen equal to the cell length following previous study in 2D [1]. Here, we first made several tests by varying the regularization length l_K. The minimal value that allowed the Gauss-Newton to converge is equal to 35 voxels which is quite near to the cell length. This reconfirms our characteristic length choice of about the cell length. For the regularization length of the boundary given
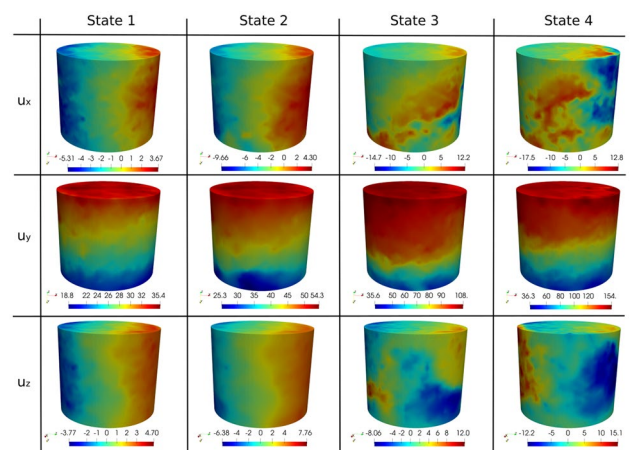

Fig. 10 Deformed macro meshes obtained with mesoscale DVC for the different loading states in addition to the global correlation score $\sigma(r)$ (which stands for the standard deviation of the residual field r defined in (equation 5))

**Fig. 11** Displacement fields (in voxels unit) obtained using mesoscale DVC and the mesh defined in Fig. 5(c)

by l_L, the choice performed in [1] and which consisted in setting l_L to its smallest value was not verified in this case. We thus proceeded by bisection with a large value of 50 voxels and gradually decreased it. l_L was finally set equal to l_K. The elastic stiffness matrix **K** of the architecture was assembled with a Young's modulus $E = 1$ and an arbitrary Poisson coefficient $\nu = 0.28$. Preliminary numerical tests showed that the algorithm has no sensitivity with respect to the Poisson ratio. In total, the mechanically regularized scheme started from the initial DVC solution obtained with the mesoscale discretization shown in Fig. 5(c). In the rest of the paper, this solution will be used as mesoscale reference when comparing the microscale with the mesoscale DVC. Concerning the computational time, the whole process (including mesoscale DVC as it is the initial guess of microscale DVC) consumed 55 GB of RAM and lasted 20 minutes. We recall that the different parameters of both mesoscale and microscale DVC are synthesized in Table 2.

Distribution of the residual field over the whole region

In order to compare quantitatively the residual maps of the DVC analyses defined on different meshes, each result was post-processed such that all residuals were expressed on the same support. More precisely, the residual maps were computed at the integration points of the micro-scale FE mesh (thus only the cellular constituent domain is considered for the study) for all DVC analyses. It requires a projection step that goes from the meso-scale mesh to the micro-scale mesh as explained in Appendix. To start comparing the two DVC approaches, we plot the histogram of the residual field in Fig. 12 along with the residual field itself, see Fig. 13. First we observe that when the correlation converges (*i.e.* for the three first loading states), the residual distribution is Gaussian with a zero mean value. We also see that the correlation accuracy decreases with the increase of the loading increments, especially when mesoscale elements are used. This can be explained by the fact that the kinematics becomes more and more complex, but the discretization is the same. The same trend can be seen on the distribution of the
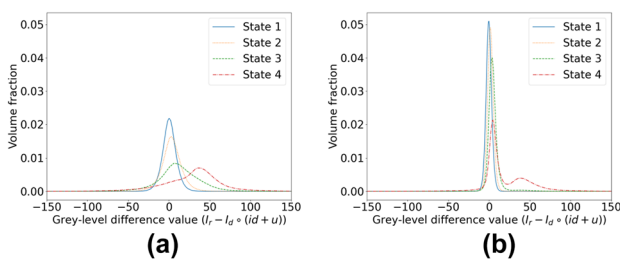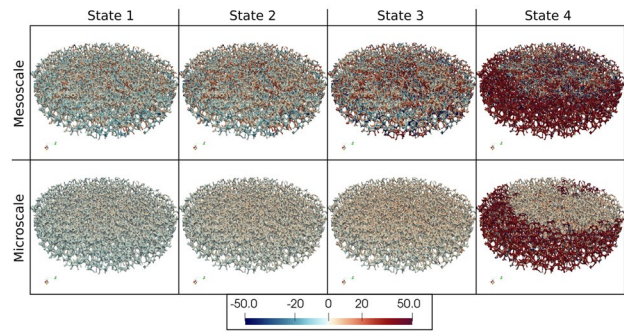
Fig. 13 Distribution of the residual field for the different loading states and for both microscale and mesoscale DVC

grey-level residual field in Fig. 13. Then, Fig. 12 shows that the standard deviation of the residual distribution is divided at least by a factor of 2 for the first and second states and by a factor of 4 for the third state for microscale DVC against mesoscale DVC. Therefore the proposed architecture-driven regularization approach definitely improves the correlation accuracy for the third state. However, with multiple initialization attempts, the fourth loading state (which has a 28.5% strain level) could not be correlated correctly. This is detected with the second peak in the histograms in Fig. 12(b) and corresponds to the large red circular region observed on Fig. 13. This failed correlation is due to the fact that the Gauss-Newton algorithm is very sensitive to the initialization and none of the proposed initialization techniques presented previously succeeded. Another source of the problem can be related to the chosen cylindrical mesh that contains the foam sample. If we look closely to the shape of the external boundary of the sample shown in Figs. 3, 8 or even 2, then we notice that the boundary is not completely straight. This induces that a large part of void was correlated in the elements which has perhaps increased the measurement uncertainty for the fourth state in this region.

Fine analysis of the measured kinematics over a local region

From now on, we only focus on the third loading state as it is the state with the most important strain level (12.3%) that we were able to compute.

In order to look for the differences between the two DVC approaches in more details, let us extract from the foam slice another small region of interest as indicated in Fig. 14. With this process, we get a planar view of the cellular region.
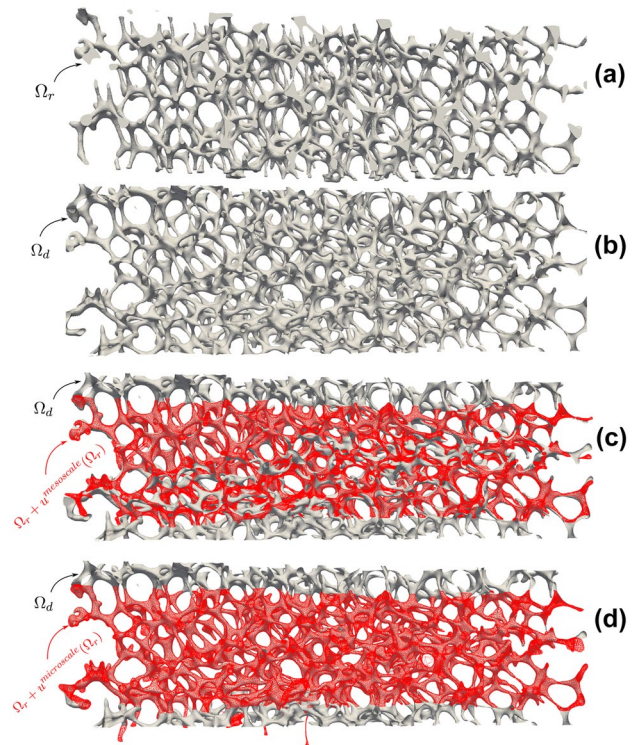
We display in Fig. 15 the obtained displacement fields in x, y, z directions (we recall that y is the compression direction) in addition to the Von Mises strain field. From a global point of view, both solutions (micro and meso) are similar. However, if we look very precisely at some struts, displacement variations are measured at the sub-cellular scale with

Fig. 12 Histogram of the residual field. (**a**) Mesoscale DVC and (**b**) Microscale DVC
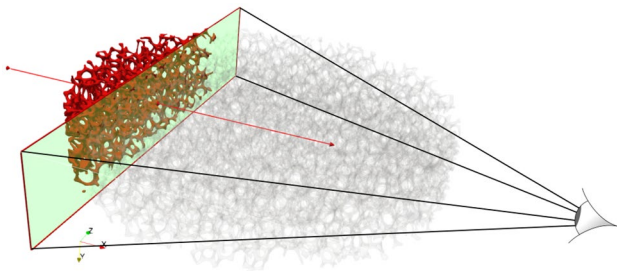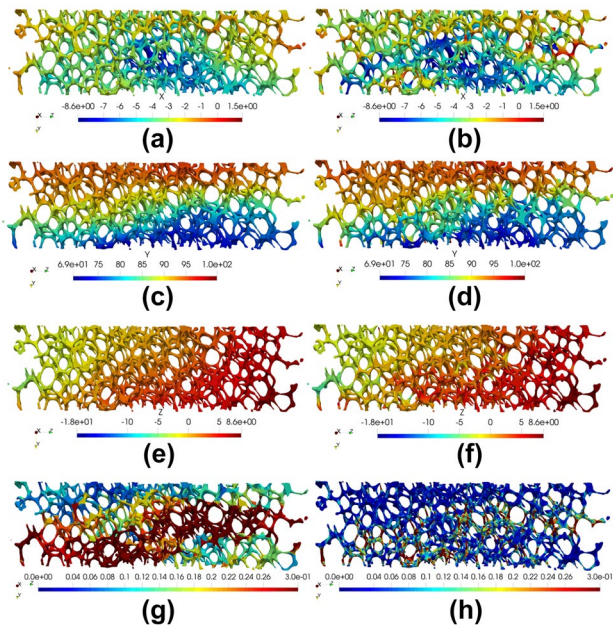
Fig. 14 Extraction of a region of analysis from the foam slice (clipping in the direction (1,0,0) with the Paraview software)

the micro approach which is not the case for the meso solution. It can be seen that the strain is homogeneous at the cell scale for the mesoscale approach, while it becomes possible to clearly locate the spans that concentrate the largest strains and bendings with the microscale counterpart. Microscale DVC makes it possible to extract much more detailed and valuable information from the same raw data.

In order to see even more clearly the differences between the mesoscale and microscale solutions, we finally proceed to a practical visualization technique as follows. As we can also segment the images of the deformed configurations, we can verify visually if the displacement field obtained by the DVC method allows to align the initial configuration on the deformed configuration. Figure 16 illustrates this verification approach. We can see in the extracted region a large


Fig. 15 Comparison of mesoscale and microscale DVC. Left: Mesoscale DVC. Right: Microscale DVC. From top to bottom: transverse displacement u_x, axial displacement u_y, transverse displacement u_z and Von Mises strain field $\varepsilon_{vm} = \|\varepsilon\|_F$ (Frobenius norm)

Fig. 16 Difference between mesoscale and microscale DVC. (**a**) Segmented image I_r, (**b**) segmented image I_d for the third loading state, (**c**) warping the reference state with the solution coming from mesoscale DVC and (**d**) warping the reference state with the solution coming from microscale DVC. Ω_r and Ω_d stand for the reference and deformed configurations respectively

number of cell struts that undergo geometric non-linearities like buckling or large deformations. We also observe some kind of localized bands. The obtained results confirm in 3D the performance of the microscale approach observed in 2D [1]. The difference between the micro and meso DVC measurements is clear: the meso solution only allows low order transformations at the cell scale and is thus completely unable to represent the complex local kinematic of each individual cell-strut. On the contrary, the developed microscale DVC does allow to properly measure the non-linear kinematic transformation of the cell-struts.

For completeness, a zoom on some regions especially where large deformations/rotations occurs is performed in Fig. 17 in order to further appreciate the differences between the meso and micro solutions. As right before, these figures consist in superimposing, on the deformed image I_d, the mesh constructed on the reference image I_r, advected by the measured displacement field. It can be seen again that the microscale approach accurately identified the large localized deformations of individual struts, whereas its mesoscale counterpart failed. This constitutes a clear evidence that the proposed elastic regularization does not act as a strong regularization that constrains the kinematic measurement in
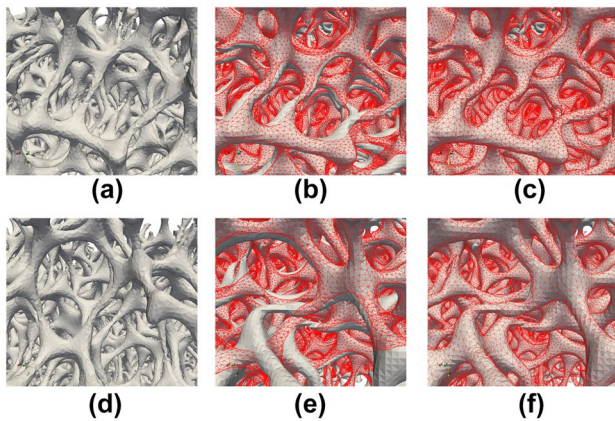
Fig. 17 (**a-d**) Two regions in the reference configuration Ω_r. (**b-e**) In grey color: Ω_d. In red color: $\Omega_r + u^{mesoscale}(\Omega_r)$. (**c-f**) In grey color: Ω_d. In red color: $\Omega_r + u^{microscale}(\Omega_r)$

the space of purely elastic solutions. Indeed, the measured displacement does not correspond at all to the elastic model used for the regularization. The regularization only consists in prescribing a local elastic behavior that allows to complement mechanically the partial measurement at the cell-scale given by standard the grey-level metric. This offers the opportunity to measure and quantify non-linear kinematics which is a novelty in experimental mechanics.

From a mechanical point of view, any DVC method (subset, finite element, possibly regularized)—if it relies on a kinematic description above the micro-structure scale—does not allow at all to represent the complex local kinematics of the material. Worse, the approach described as meso here shows that the individual struts deform in tension/compression (see Fig. 17(e)), while they clearly deform in bending. This is due to the simple fact that the chosen mesoscopic kinematics (required because of the lack of texture at the lower scale) is too poor. On the contrary, the proposed method describes the local bending kinematics (see Fig. 17(f)), for each individual beam. Not only the type of mechanism (stretching-dominated versus bending dominated) is well identified but the amplitude of the deformation of each beam is accurately measured. We can see that the proposed tool allows a much better quality measurement and avoids misinterpretation of the class of dominance involved in crushing.

Conclusion and Perspectives

In this study, an *in-situ* compression test was performed in an X-ray μ-CT scanner on an open cell polyurethane foam. Two DVC frameworks were developed. A first global FE-DVC based on large finite elements that do not take into account the underlying architecture only allowed to obtain a mesoscale and homogenized displacement/strain field. It was shown that this

approach reaches its limits when localized complex subcellular kinematics occur. From a mechanical point of view, this type of meso analysis does not allow to analyze the nature of the mechanisms involved in the crushing of architected materials. Indeed, this mesoscopic measurement suggests that the beams deform in tension/compression and the dominance type is stretching. It is therefore impossible to exploit classic DVC measurements at the scale of the architecture. The kinematic model used to measure the displacements is too poor and it is not possible to consider richer approximation spaces due to the absence of lower scale texture. In order to tackle this problem, we make use of an architecture driven mechanical regularization of DVC. More precisely, the measurement support is a sample-specific image-based finite element mesh that describes the cellular architecture. Provided the correct setting of the parameters like grey-level threshold, mesh refinement–here related to voxel size–, geometric approximation and regularization, regularization parameter–here related to the mean cell length and fixed from a previous two-dimensional L-curve study, see again [1]– the proposed microscale DVC, made it possible to measure accurately particularly complex three-dimensional kinematics (such as buckling or bending) in the absence of pattern at the strut scale. The efforts on the implementation allowed to treat a real, representative case (with several millions of degrees of freedom). This approach was able to measure, in the volume, local displacements and deformations of high complexity. Not only the type of deformation dominance (stretching-dominated versus bending dominated) was correctly identified but the amplitude and location of the deformations of each beam is perfectly reproduced. This tool is intended to be used for the analysis of local deformation mechanisms during *in-situ* tests.

Although the method was capable of providing accurate measurements of individual strut of a foam sample in compression, there are still a number of areas for improvement.

As explained above, the threshold used for segmentation was chosen so that the volume fraction of the image-based model approximated as closely as possible the porosity of the foam as specified by the supplier. It would be interesting to further investigate the effect of this choice.

In order to reduce the geometric errors related to noise and poor resolution (imposed by the imaging tool), it would be interesting to perform high resolution scans of the studied samples with high energy μ-CT scanners (for example using Synchrotron sources) so that a reference geometry in which a high trust is placed can be set once for all [57]. From this reference image, one can build faithful geometries for both the simulation and correlation aspects. For correlation, one can go back to conventional μ-CT scanners in order to perform *in-situ* tests.

The uncertainties at top and bottom boundary nodes seem higher than in the bulk. To reduce the region of interest, only a section of the image was analysed. Some struts may

have been cut in two in the thickness, resulting in very small weakly connected elements. The associated stiffness can be very low and so the regularization. This higher uncertainty on the edges does not have a strong effect on the measurement but would require further developments such as improving the boundary regularization [32].

Among other perspectives, a very interesting avenue concerns the regularization operator. It is indeed possible, with exactly the same formalism, to consider more advanced models (in particular non-linear ones) [73]. In particular, it would be interesting to update the constitutive parameters and the geometry stiffness of the regularization model, which is possible within the very same framework [37, 73].

The problem of high performance computing for regularized DVC is of double difficulty. First, from a memory point of vue, the equilibrium gap regularization increases the numerical cost of the DVC algorithm as the number of extra diagonals increases in the left hand side of the resolved linear system. The computational cost issue may become a real concern in three dimensions. Domain decomposition techniques or model reduction techniques could then be used advantageously [41, 54, 55]. In addition, adequate iterative solvers must be adapted for the special Gauss-Newton algorithm of DVC [74].

One of the most difficult aspects in image correlation is the accurate initialization of the gradient-based optimization scheme. Even though coarse to fine and reduced basis approaches seem to be sufficient in many applications, their use is quite manual and heuristic in the sense that multiple attempts are performed before running the final correlation. Another prospect of this work would be to investigate other robust initialization strategies [75].

Appendix: FE interrogation for arbitrary points

We present in this appendix a procedure that allows to perform automatically the displacement exchange between two arbitrary finite-element meshes. We consider the following steps for solving this geometric problem:

Step 1: Location of the Nearest Face of the FE Mesh to the Point

Efficient data structures (very common in collision detection algorithms) can be efficiently used to speed up point queries with respect to complex geometric objects represented by faces. In this work, we mainly use a rootine from the CGAL library [69] and PyMesh [76]. Efficient point queries such as intersections, distance computation, ray shooting can be performed using Axis Aligned Bounding Boxes (AABB) trees [77]. This allows to detect the nearest face to an arbitrary point.

Step 2: Location of the Tetrahedral Element Containing the Point

After determining the nearest face, the location test is performed on the tetrahedrons that share this same face (they are at most two). To do so, one can consider two methods:

- **Method 1**: Computation of the barycentric coordinates by resolution of the linear system:

$$
\begin{cases}
x = \sum_{i=1}^{m} \lambda_i t_i \\
\sum_{i=1}^{m} \lambda_i = 1
\end{cases}
\tag{12}
$$

If $\lambda_i > 0, \quad \forall i \in \{1, ..., m\}$ then the point x belongs to the tetrahedron bounded by the nodes $(t_i)_{i \in \{1,...,m\}}$. m is the number of nodes per convex set (4 in our case).

- **Method 2**: A faster method which does not consist in solving a linear system can be considered. We only evaluate the signed distance of the point to each of the tetrahedron faces. First, the orientation of the faces must be determined so that all the face normal vectors point towards the same direction. This is given by an orientation matrix denoted $\mathbf{O} \in \mathbb{R}^{3 \times 4}$ that depends of the used mesh. Each column of $\mathbf{O}$ represents the indices of the nodes of the tetrahedron faces. The point x belongs to the tetrahedron if the distances to all the faces have the same sign. This is written as follows:

$$
(x - t_{\mathbf{O}_{2,i}})^T n_i(t_{\mathbf{O}_{2,i}}) < 0, \quad \forall i \in \{1, .., 4\}
\tag{13}
$$

where $n_i(t_{\mathbf{O}_{2,i}})$ is the normal vector at node $t_{\mathbf{O}_{2,i}}$ (which is the second node of the face i). It is defined by $n_i(t_2) = (t_{\mathbf{O}_{2,i}} - t_{\mathbf{O}_{1,i}}) \times (t_{\mathbf{O}_{3,i}} - t_{\mathbf{O}_{2,i}})$.

Step 3: Evaluation of the Displacement Field at the Point

Once the tetrahedron containing the point is determined, the isoparametric transformation ($x = \sum_i N_i(\xi) t_i$) is inverted in order to find the isoparametric coordinate ξ of the point x. The finite element interpolation formula can afterwards be applied to evaluate the desired displacement field ($u^{fine}(x) = \sum_i N_i(\xi) u^{coarse}(t_i)$), where t_i are again the nodes of the tetrahedron.

Declarations

Conflicts of Interest The authors declare that they have no known competing financial interests or personal relationships that could have appeared to influence the work reported in this paper.

References

1. Rouwane A, Bouclier R, Passieux JC, Périé JN (2022) Architecture-driven digital image correlation technique (ADDICT) for the measurement of sub-cellular kinematic fields in speckle-free cellular materials. Int J Solids Struct 234–235

2. Ashby M (2013) Designing architectured materials. Scripta Mater 68(1):4–7

3. Brechet Y, Embury JD (2013) Architectured materials: Expanding materials space. Scripta Mater 68(1):1–3

4. Greer JR, Deshpande VS (2019) Three-dimensional architected materials and structures: Design, fabrication, and mechanical behavior. MRS Bull 44(10):750–757

5. Dallago M, Winiarski B, Zanini F, Carmignato S, Benedetti M (2019) On the effect of geometrical imperfections and defects on the fatigue strength of cellular lattice structures additively manufactured via selective laser melting. Int J Fatigue 124:348–360

6. Hernández-Nava E, Smith C, Derguti F, Tammas-Williams S, Leonard F, Withers P, Todd I, Goodall R (2016) The effect of defects on the mechanical response of ti-6al-4v cubic lattice structures fabricated by electron beam melting. Acta Materialia 108:279–292

7. Maire E, Fazekas A, Salvo L, Dendievel R, Youssef S, Cloetens P, Letang JM (2003) X-ray tomography applied to the characterization of cellular materials. related finite element modeling problems. Compos Sci Technol 63(16):2431–2443 Porous Materials

8. van Rietbergen B, Weinans H, Huiskes R, Odgaard A (1995) A new method to determine trabecular bone elastic properties and loading using micromechanical finite-element models. J Biomech 28(1):69–81

9. Frey P, Sarter B, Gautherie M (1994) Fully automatic mesh generation for 3-d domains based upon voxel sets. Int J Numer Meth Eng 37(16):2735–2753

10. Hollister S, Brennan J, Kikuchi N (1994) A homogenization sampling procedure for calculating trabecular bone effective stiffness and tissue level stress. J Biomech 27(4):433–444

11. Ulrich D, van Rietbergen B, Weinans H, Rüegsegger P (1998) Finite element analysis of trabecular bone structure: a comparison of image-based meshing techniques. J Biomech 31(12):1187–1192

12. Lozanovski B, Leary M, Tran P, Shidid D, Qian M, Choong P, Brandt M (2019) Computational modelling of strut defects in slm manufactured lattice structures. Materials & Design 171

13. Müller R, Rüegsegger P (1995) Three-dimensional finite element modelling of non-invasively assessed trabecular bone structures. Med Eng Phys 17(2):126–133

14. Buffiere JY, Maire E, Adrien J, Masse JP, Boller E (2010) *In situ* experiments with x ray tomography: an attractive tool for experimental mechanics. Exp Mech 50(3):289–305

15. Bay BK, Smith TS, Fyhrie DP, Saad M (1999) Digital volume correlation: three-dimensional strain mapping using x-ray tomography. Exp Mech 39(3):217–226

16. Chen Y, DallÁra E, Sales E, Manda K, Wallace R, Pankaj P, Viceconti M (2017) Micro-ct based finite element models of cancellous bone predict accurately displacement once the boundary condition is well replicated: A validation study. J Mech Behav Biomed Mater 65:644–651

17. Rannou J, Limodin N, Réthoré J, Gravouil A, Ludwig W, Baïetto-Dubourg MC, Buffiëre JY, Combescure A, Hild F, Roux S (2010) Three dimensional experimental and numerical multiscale analysis of a fatigue crack. Comput Meth Appl Mech Eng 199(21):1307–1325, multiscale Models and Mathematical Aspects in Solid and Fluid Mechanics

18. Zauel R, Yeni Y, Bay B, Dong X, Fyhrie DP (2006) Comparison of the linear finite element prediction of deformation and strain of human cancellous bone to 3d digital volume correlation measurements. J Biomech Eng 128(1):1–6

19. Buljac A, Trejo Navas VM, Shakoor M, Bouterf A, Neggers J, Bernacki M, Bouchard PO, Morgeneyer TF, Hild F (2018) On the calibration of elastoplastic parameters at the microscale via x-ray microtomography and digital volume correlation for the simulation of ductile damage. Eur J Mech A Solids 72:287–297

20. Marter AD, Dickinson AS, Pierron F, Browne M (2018) A practical procedure for measuring the stiffness of foam like materials. Exp Tech 42(4):439–452

21. Salvo L, Belestin P, Maire E, Jacquesson M, Vecchionacci C, Boller E, Bornert M, Doumalin P (2004) Structure and mechanical properties of afs sandwiches studied by *in-situ* compression tests in x-ray microtomography. Adv Eng Mater 6(6):411–415

22. Bastawros AF, Bart-Smith H, Evans A (2000) Experimental analysis of deformation mechanisms in a closed-cell aluminum alloy foam. J Mech Phys Solids 48(2):301–322

23. Hu Z, Du Y, Luo H, Zhong B, Lu H (2014) Internal deformation measurement and force chain characterization of mason sand under confined compression using incremental digital volume correlation. Exp Mech 54(9):1575–1586

24. Verhulp E, Rietbergen B, Huiskes R (2004) A three-dimensional digital image correlation technique for strain measurements in microstructures. J Biomech 37(9):1313–1320

25. Roux S, Hild F, Viot P, Bernard D (2008) Three-dimensional image correlation from x-ray computed tomography of solid foam. Compos Part A: Appl Sci Manufac 39(8):1253–1265

26. DallÁra E, Peña-Fernández M, Palanca M, Giorgi M, Cristofolini L, Tozzi G (2017) Precision of digital volume correlation approaches for strain analysis in bone imaged with micro-computed tomography at different dimensional levels. Frontiers in Materials 4:31

27. Leclerc H, Périé JN, Roux S, Hild F (2011) Voxel-scale digital volume correlation. Exp Mech 51(4):479–490

28. Réthoré J, Roux S, Hild F (2009) An extended and integrated digital image correlation technique applied to the analysis of fractured samples. European Journal of Computational Mechanics 18(3–4):285–306

29. Fischer B, Modersitzki J (2004) A unified approach to fast image registration and a new curvature based registration technique. Linear Algebra Appl 380:107–124

30. Sotiras A (2011) Discrete image registration: a hybrid paradigm. PhD thesis, Ecole Centrale Paris

31. Claire D, Hild F, Roux S (2004) A finite element formulation to identify damage fields: the equilibrium gap method. Int J Numer Meth Eng 61(2):189–208

32. Mendoza A, Neggers J, Hild F, Roux S (2019) Complete mechanical regularization applied to digital image and volume correlation. Comput Methods Appl Mech Eng 355:27–43

33. Deshpande V, Ashby M, Fleck N (2001) Foam topology: bending versus stretching dominated architectures. Acta Mater 49(6):1035–1040. https://doi.org/10.1016/S1359-6454(00)00379-7

34. Somera A, Poncelet M, Auffray N, Réthoré J (2022) Quasi-periodic lattices: Pattern matters too. Scripta Materialia 209:114378 https://doi.org/10.1016/j.scriptamat.2021.114378

35. Ahrens J, Geveci B, Law C (2005) Paraview: An end-user tool for large data visualization. The visualization handbook 717(8)

36. Ayachit U (2015) The paraview guide: a parallel visualization application

37. Réthoré J (2010) A fully integrated noise robust strategy for the identification of constitutive laws from digital images. Int J Numer Meth Eng 84(6):631–660

38. Leclerc H, Périé JN, Hild F, Roux S (2012) Digital volume correlation: what are the limits to the spatial resolution ? Mechanics & Industry 13(6):361–371

39. Horn BKP, Schunck BG (1981) Determining optical flow. Artif Intell 17(1–3):185–203

40. Leclerc H, Roux S, Hild F (2015) Projection savings in ct-based digital volume correlation. Exp Mech 55(1):275–287

41. Gomes Perini L, Passieux JC, Périé JN (2014) A multigrid pgd-based algorithm for volumetric displacement fields measurements. Strain 50(4):355–367

42. Neggers J, Blaysat B, Hoefnagels JPM, Geers MGD (2016) On image gradients in digital image correlation. Int J Numer Meth Eng 105(4):243–260

43. Passieux JC, Bouclier R (2019) Classic and inverse compositional gauss-newton in global DIC. Int J Numer Meth Eng 119(6):453–468

44. Fedele R, Galantucci L, Ciani A (2013) Global 2d digital image correlation for motion estimation in a finite element framework: a variational formulation and a regularized, pyramidal, multi-grid implementation. Int J Numer Meth Eng 96(12):739–762

45. Pan B, Xie H, Wang Z, Qian K, Wang Z (2008) Study on subset size selection in digital image correlation for speckle patterns. Opt Express 16(10):7037–7048

46. Bomarito G, Hochhalter J, Ruggles T, Cannon A (2017) Increasing accuracy and precision of digital image correlation through pattern optimization. Opt Lasers Eng 91:73–85

47. Fouque R, Bouclier R, Passieux JC, Périé JN (2021) Fractal pattern for multiscale digital image correlation. Exp Mech 61(3):483–497

48. Passieux JC, Périé JN, Marguerès P, Douchin B, Gomes Perini L (2013) On the joint use of an opacifier and digital volume correlation to measure micro-scale volumetric displacement fields in a composite. In: ICTMS2013 - The 1st International Conference on Tomography of Materials and Structures, Ghent, Belgium

49. Brault R, Germaneau A, Dupré JC, Doumalin P, Mistou S, Fazzini M (2013) *In-situ* analysis of laminated composite materials by X-ray micro-computed tomography and digital volume correlation. Exp Mech 53(7):1143–1151

50. Xu F (2018) Quantitative characterization of deformation and damage process by digital volume correlation: A review. Theor Appl Mech Lett 8(2):83–96

51. Dufour JE, Beaubier B, Hild F, Roux S (2015) Cad-based displacement measurements with stereo-dic. Exp Mech 55(9):1657–1668

52. Colantonio G, Chapelier M, Bouclier R, Passieux JC, Marenić E (2020) Noninvasive multilevel geometric regularization of mesh-based three-dimensional shape measurement. Int J Numer Meth Eng 121(8):1877–1897

53. Chapelier M, Bouclier R, Passieux JC (2021) Free-form deformation digital image correlation (ffd-dic): A non-invasive spline regularization for arbitrary finite element measurements. Comput Methods Appl Mech Eng 384

54. Bouclier R, Passieux JC (2017) A domain coupling method for finite element digital image correlation with mechanical regularization: Application to multiscale measurements and parallel computing. Int J Numer Meth Eng 111(2):123–143

55. Passieux JC, Périé JN (2012) High resolution digital image correlation using proper generalized decomposition: Pgd-dic. Int J Numer Methods Eng 92(6):531–550

56. van Dijk NP, Wu D, Persson C, Isaksson P (2019) A global digital volume correlation algorithm based on higher-order finite elements: Implementation and evaluation. Int J Solids Struct 168:211–227

57. Tsitova A, Bernachy-Barbe F, Bary B, Dandachli S, Bourcier C, Smaniotto B, Hild F (2021) Damage quantification via digital volume correlation with heterogeneous mechanical regularization: Application to an *in situ* meso-flexural test on mortar. Exp Mech pp. 1–17

58. Unser M (1999) Splines: a perfect fit for signal and image processing. IEEE Signal Process Mag 16(6):22–38

59. Unser M, Aldroubi A, Eden M et al (1991) Fast b-spline transforms for continuous image representation and interpolation. IEEE Trans Pattern Anal Mach Intell 13(3):277–285

60. Jones EM, Iadicola MA etal (2018) A good practices guide for digital image correlation. International Digital Image Correlation Society 10

61. Bajcsy R, Kovačič S (1989) Multiresolution elastic matching. Computer vision, graphics, and image processing 46(1):1–21

62. Rueckert D, Sonoda LI, Hayes C, Hill DL, Leach MO, Hawkes DJ (1999) Nonrigid registration using free-form deformations: application to breast mr images. IEEE Trans Med Imaging 18(8):712–721

63. Haber E, Modersitzki J (2006) A multilevel method for image registration. SIAM J Sci Comput 27(5):1594–1607

64. Réthoré J, Hild F, Roux S (2007) Shear-band capturing using a multiscale extended digital image correlation technique. Comput Methods Appl Mech Eng 196(49–52):5016–5030

65. Fedele R, Ciani A, Galantucci L, Bettuzzi M, Andena L (2013) A regularized, pyramidal multi-grid approach to global 3d-volume digital image correlation based on x-ray micro-tomography. Fund Inform 125(3–4):361–376

66. Valmalle M, Vintache A, Smaniotto B, Gutmann F, Spagnuolo M, Ciallella A, Hild F (2022) Local-global dvc analyses confirm theoretical predictions for deformation and damage onset in torsion of pantographic metamaterial. Mech Mater p. 104379

67. Lorensen WE, Cline HE (1987) Marching cubes: A high resolution 3d surface construction algorithm. Computer Graphics 21(4):163–169

68. van der Walt S, Schünberger JL, Nunez-Iglesias J, Boulogne F, Warner JD, Yager N, Gouillart E, Yu T (2014) scikit-image: image processing in Python. PeerJ 2

69. The CGAL Project (2021) CGAL user and reference manual. https://doc.cgal.org/5.3.1/Manual/packages.html

70. Szeliski R, Lavallée S (1996) Matching 3-d anatomical surfaces with non-rigid deformations using octree-splines. Int J Comput Vis 18(2):171–186

71. Ferrant M, Warfield SK, Guttmann CR, Mulkern RV, Jolesz FA, Kikinis R (1999) 3d image matching using a finite element based elastic deformation model. In: International Conference on Medical Image Computing and Computer-Assisted Intervention, Springer, pp 202–209

72. Chen Y, Davis TA, Hager WW, Rajamanickam S (2008) Algorithm 887: Cholmod, supernodal sparse cholesky factorization and update/downdate. ACM Transactions on Mathematical Software (TOMS) 35(3):1–14

73. Réthoré J, Muhibullah Elguedj T, Coret M, Chaudet P, Combescure A (2013) Robust identification of elasto-plastic constitutive law parameters from digital images using 3d kinematics. Int J Solids Struct 50(1):73–85

74. Tournier PH, Aliferis I, Bonazzoli M, De Buhan M, Darbas M, Dolean V, Hecht F, Jolivet P, El Kanfoud I, Migliaccio C et al (2019) Microwave tomographic imaging of cerebrovascular accidents by using high-performance computing. Parallel Comput 85:88–97

75. MacNeil JML, Morozov D, Panerai F, Parkinson D, Barnard H, Ushizima D (2019) Distributed global digital volume correlation by optimal transport. In: 2019 IEEE/ACM 1st Annual Workshop

on Large-scale Experiment-in-the-Loop Computing (XLOOP), IEEE, pp 14–19

76. PyMesh DT (2020) Pymesh: geometry processing library for python. https://github.com/PyMesh/PyMesh

77. Akenine-Mller T, Haines E, Hoffman N (2018) Real-time Rendering, Fourth Edition, 4th edn. A. K, Peters Ltd, USA

Publisher's Note Springer Nature remains neutral with regard to jurisdictional claims in published maps and institutional affiliations.